Loudspeaker Virtualization–Part II: The Inverse Transducer Model and the Direct-Inverse-Direct Chain

Alberto Bernardini[a,*], Lucio Bianchi[b], Augusto Sarti[a]

[a] *Dipartimento di Elettronica, Informazione e Bioingegneria (DEIB), Politecnico di Milano, Piazza L. Da Vinci 32, 20133 Milano, Italy*
[b] *Elettromedia s.p.a., Strada Regina km 3.500, 62018 Potenza Picena (MC), Italy*

Abstract

This manuscript, the second of a two-part series, shows how a discrete-time circuital model of loudspeakers, which is extensively analyzed in the first part, can be exploited to develop a method for loudspeaker virtualization. This method can be used to alter the behavior of a physical loudspeaker in such a way to match that of a target loudspeaker. Examples of applications include loudspeaker equalization or linearization. The method is characterized by a structure called Direct-Inverse-Direct Chain, which is composed of three blocks: a digital model of the target loudspeaker; a digital model of the inverse loudspeaker; and the physical loudspeaker. The inverse loudspeaker model is derived from the equivalent circuit of the direct system using a two-port element known in circuit theory as "nullor". We show how this inverse model can be efficiently implemented in the discrete-time domain with no iterative solvers by exploiting Wave Digital Filter principles. The proposed virtualization algorithm is extensively tested both through simulations and applications to real loudspeakers. In particular, we show how the algorithm can reduce the distortion of the transducer output pressure signal, and how it can make a loudspeaker sound like a target loudspeaker with a desired nonlinear behavior.

*Corresponding author
Email addresses: alberto.bernardini@polimi.it (Alberto Bernardini), lucio.bianchi@elettromedia.it (Lucio Bianchi), augusto.sarti@polimi.it (Augusto Sarti)

Keywords: Nonlinear Inverse Loudspeaker Models, Loudspeaker Virtualization
2010 MSC: 00-01, 99-00

1. Introduction

Loudspeakers are transducers that convert electrical audio signals into sound waves. This transduction process is, in fact, nonlinear and it may introduce several modifications in the output signal, which are typically manifested as alterations of the frequency content and distortions [1]. As this is an undesired behavior in many application scenarios, algorithms have been proposed and developed to preprocess the audio signal for the purpose of reducing the impact of nonidealities in the electroacoustic transduction [2].

In particular, many digital signal processing methods have been proposed for loudspeaker linearization. The most traditional approach relies on feedback linearization [3], recently reformulated based on output flatness and trajectory planning [4, 5]. To overcome the limitations of feedback-based approaches, open-loop alternatives have emerged starting from the seminal works by Klippel [6]. Among open-loop methods, we can identify contributions based on a black-box modeling approach [7, 8, 9] and contributions based on a signal processing inverse of the nonlinear physical model [6, 10, 11, 12, 13]. Moreover, a family of hybrid methods have been investigated, where the feedback signals are computed as the output of nonlinear models of the system [14, 15].

Other works in the literature focus on the problem of designing digital equalization techniques for loudspeaker systems [6, 16, 17]. Similarly to the aforementioned loudspeaker linearization approaches, these methods consist of inserting a digital filter before the electroacoustic transducer.

In fact, both loudspeaker linearization and loudspeaker equalization problems can be thought of as particular cases of the more general problem of forcing a desired transduction behavior into the loudspeaker without altering its physical and geometrical components. We refer to this general task of modifying

the behavior of a physical loudspeaker, through digital signal preprocessing algorithms, in such a way to match that of a target loudspeaker, as *loudspeaker virtualization*.

In this manuscript we present a novel methodology for loudspeaker virtualization that is based on the design and the efficient digital implementation of the inverse circuital model of a loudspeaker electrical equivalent. The lumped loudspeaker model that we consider for this purpose has been extensively described in the first part of this work [18] and it will be called the *Direct System*. It is composed of three subcircuits covering the electrical domain, the mechanical domain, and the acoustic domain of the transducer, respectively. The input signal of the *Direct System* is the input voltage applied to the coil of the transducer, while the output signal is the voltage across the acoustic impedance of the model, corresponding to a pressure signal. We show how the *Inverse System*, i.e., the *exact* inverse of the nonlinear *Direct System*, can be readily designed by properly adding an ideal two-port circuit element, known in circuit theory as *nullor* [19], to the circuit of the *Direct System*.

We then discuss how the nonlinear *Direct System* described in [18] and the *Inverse System* presented in this manuscript can be combined to perform loudspeaker virtualization. As examples of applications of the proposed approach, we show how the designed precompensation algorithm can reduce the distortion of the transducer output pressure signal, and how it can make a loudspeaker sound like a target loudspeaker with a desired nonlinear behavior.

It is important to underline that the methodological approach that we present in this article can be adopted to design the inverse of any physical model that is formulated in the form of an equivalent circuit. We will show that the inversion that we achieve is exact, therefore the validity of this approach can only be limited by the validity of the circuital model itself.

The discrete-time implementation of the *Inverse System* that we propose is based on the same principles of Wave Digital Filter (WDF) theory [20, 21, 22, 23], used for implementing the *Direct System* in [18], and it is *fully explicit*, which means that it does not rely on any iterative solver.

This manuscript is a continuation of [18], although it has been organized in such a way to be as self-contained as possible. Section 2 provides the background on a general inversion theorem [24] that, given a *Direct System* represented as a circuit with an input signal and an output signal characterized by a one-to-one relation, allows us to design the inverse of the *Direct System* by properly connecting a nullor to the *Direct System* circuit. Given the nonlinear loudspeaker model described in [18], Section 3 shows how to apply the inversion theorem discussed in Section 2 in order to derive the circuit of the inverse loudspeaker system. Section 4 presents an explicit WDF implementation of the inverse loudspeaker system. Section 5 describes the proposed loudspeaker virtualization algorithm. In particular, the algorithm is based on the so called *Direct-Inverse-Direct Chain* (DIDC) that is composed of: one digital filter block implementing the direct target loudspeaker system, one digital filter block implementing the inverse loudspeaker system, and a physical block representing the real direct system, i.e., the actual loudspeaker. Section 6 shows how the proposed DIDC-based approach can be employed for loudspeaker linearization. The effectiveness of the method is verified both through simulations and the application of the algorithm to two real loudspeakers; moreover, an analysis of algorithm performance degradation in presence of model parameter uncertainty is performed. Section 7 presents a further application of the proposed DIDC-based virtualization approach in which a target distortion behavior is imposed to two different real loudspeakers. Section 8 concludes this manuscript.

2. Background on the Nullor-based Inversion of Nonlinear Systems

In this Section we revise a general method presented in [24] to derive the inverse of a reference *Direct System* represented as a linear or nonlinear electrical circuit. The inversion method makes use of an ideal two-port circuit element called *nullor*, which is widely used in the literature of circuit theory to develop ideal representations of multi-port elements such as operational amplifiers or transistors [19, 25].

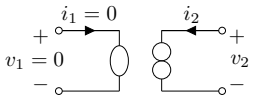

Figure 1: A nullor consisting of a nullator (represented with an ellipse) paired with a norator (represented with two contiguous circles).

Hereafter we provide some background on nullors, followed by a reformulation of the theorem on which the nullor-based inversion method relies on.

2.1. Background on Nullors

A nullor [19] is a theoretical linear two-port circuit element composed of two one-ports: the *nullator* and the *norator*. Fig. 1 shows its graphical symbol, where the ellipse represents the nullator, while the pair of adjacent circles represents the norator. The nullator can be thought of as simultaneously an open and a short circuit, as both its port current and port voltage are identically zero. Conversely, the norator is a nonreciprocal one-port with arbitrary port voltage and current. The constitutive equation of a nullor is therefore

$$\begin{bmatrix} v_1 \\ i_1 \end{bmatrix} = \begin{bmatrix} 0 & 0 \\ 0 & 0 \end{bmatrix} \begin{bmatrix} v_2 \\ i_2 \end{bmatrix} \quad , \tag{1}$$

where v_1 is the voltage across the nullator, v_2 is the voltage across the norator, i_1 is the current through the nullator and i_2 is the current through the norator.

Nullors are widely used to build ideal macromodels of more complex multiports, such as operational amplifiers (opamps), transconductance amplifiers or transistors [19, 25, 26, 27]. For example, an ideal opamp can be modeled using a nullor as shown in Fig. 2, where v_{1+}, v_{1-} and v_{2+} are the potentials at the two input terminals and the output terminal of the opamp, respectively [26].

2.2. Inversion Theorem

Techniques for implementing inverse circuital models have been explored in the literature [28, 29], especially with the purpose of developing synchronization methods for chaotic systems [30]. A generalization of the inverse circuit

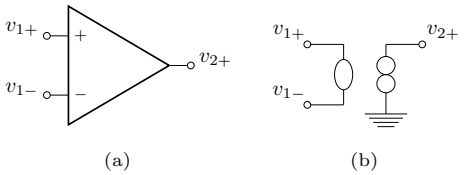

Figure 2: (a) represents an ideal opamp, while (b) is an equivalent nullor-based representation of the same ideal opamp in (a).

approach used in [28, 29] was proposed in [24], to design the inverse of a circuital system containing at least one nullor. The theorem presented in [24] is here reformulated in similar fashion as in [31].

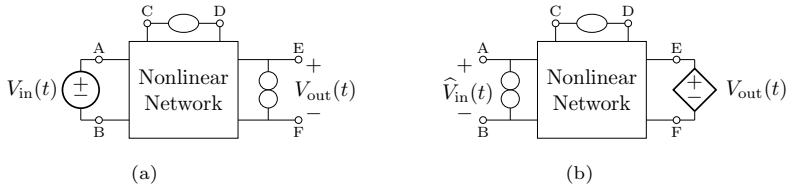

Figure 3: (a) shows the *Direct System*. The input signal $V_{\text{in}}(t)$ drives a voltage source, while the output signal $V_{\text{out}}(t)$ is the voltage across the norator. (b) shows the inverse of the system in (a). Letters A, B, C, D, E, and F indicate the same nodes of the nonlinear network both in (a) and (b).

We refer to the system to be inverted as *Direct System*, and we assume that it can be represented as in Fig. 3(a), where the *Direct System* is made of a generic linear or nonlinear non-autonomous network, with at least one nullator-norator pair connected to it. A single input signal $V_{\text{in}}(t)$ is injected into the system using a voltage source, while the output signal $V_{\text{out}}(t)$ is the voltage measured across the norator. The *Inverse System*, shown in Fig. 3(b), is obtained by replacing the input voltage source of the *Direct System* with the norator; and the norator with a voltage-controlled voltage source, whose control signal is $V_{\text{out}}(t)$. For the circuits in Fig. 3, we can state the following theorem:

Theorem 1. If the two nonlinear dynamical systems in Fig. 3 have unique bounded solutions, then, for any pair of signals $V_{in}(t)$ and $V_{out}(t)$, the system in Fig. 3(b) is the inverse of the system in Fig. 3(a). This means that for any

input signal $V_{in}(t)$ *and every initial state vector* $\mathbf{x}(0)$ *for the Direct System in Fig. 3(a), there is an initial state vector* $\widehat{\mathbf{x}}(0)$ *for the Inverse System in Fig. 3(b) such that* $\widehat{V}_{in}(t) = V_{in}(t)$.

In other words, less formally, we can state that, under the conditions expressed in *Theorem 1*, if the input of the *Inverse System* is the output of the *Direct System*, then the output of the *Inverse System* equals the input of the *Direct System*. A formulation and a proof of *Theorem 1* are offered in Section 3 of [24]. A reworded version of the same theorem is offered in [31].

3. Nonlinear Inverse Model of the Loudspeaker

Let us consider the equivalent circuit of the nonlinear *Direct System* modeling the transduction process of the loudspeaker, extensively described in the first part of this two-part work [18] and shown in Fig. 4. The electrical input voltage V_{in} and the acoustic pressure signal P_{out} (which is a voltage in the circuital model) are the input and the output of the system, respectively. Since a nullator and a norator in series are equivalent to an open circuit [26], we can add them to the circuit in Fig. 4 without altering its behavior. The result is the circuit shown in Fig. 5, which is fully equivalent to that of Fig. 4. We can now use Theorem 1 by Leuciuc [24], discussed in Section 2, to obtain the circuit shown in Fig. 6, which represents the inverse system of that in Fig. 5 and also of that of Fig. 4. It is evident from Fig. 6 that the input of the *Inverse System* is the acoustic pressure signal P_{out} driving the voltage source, while the output is the voltage $\widehat{V}_{\text{in}}$. Notice that, according to the properties of the nullator [19, 26], we have that $P_{\text{al}} = P_{\text{out}}$. Considering an ideal operational amplifier modeled as in Fig. 2, the circuit of Fig. 6 can be redrawn as in Fig. 7. Therefore, under the assumption that the operational amplifier is ideal, the two circuits in Fig. 6 and Fig. 7 are equivalent.

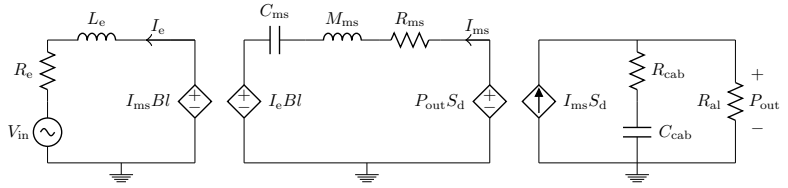

Figure 4: Circuital model of the nonlinear *Direct System*.

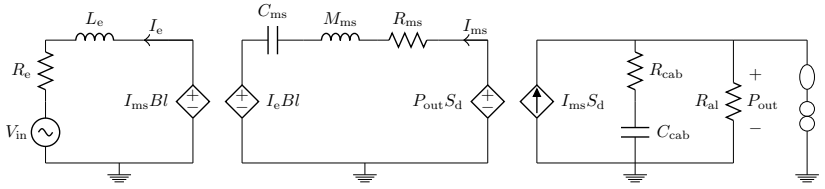

Figure 5: Circuital model of the nonlinear *Direct System* augmented with a nullor. This circuit is equivalent to the one in Fig. 4.

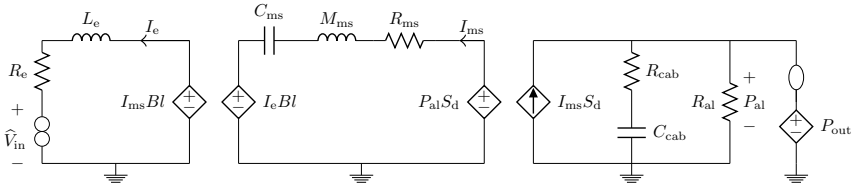

Figure 6: Circuital model of the nonlinear *Inverse System* with nullor.

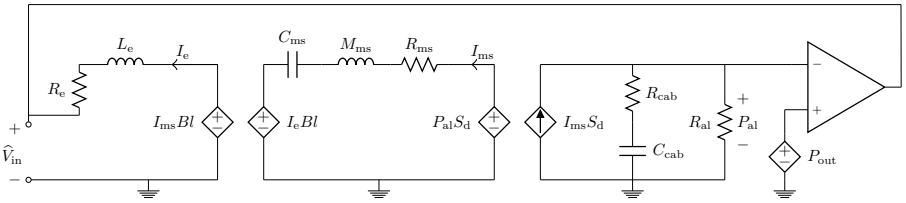

Figure 7: Circuital model of the nonlinear *Inverse System* with opamp. If the opamp is ideal, the circuit is equivalent to the one in Fig. 6.

4. Wave Digital Realization of the Nonlinear Inverse System

The WDF realization of the *Inverse System* shares many aspects with the one of the *Direct System* characterized by the circuit in Fig. 4 and extensively discussed in [18].

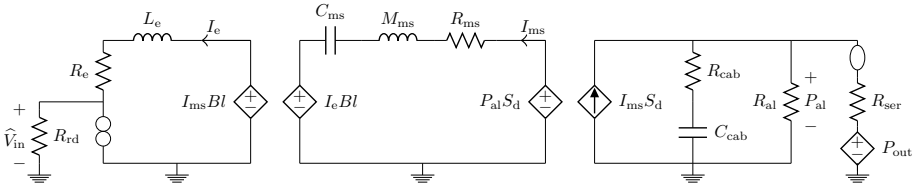

Figure 8: Circuital model of the nonlinear *Inverse System* with nullor and added resistors R_{rd} and R_{ser}. Because of the properties of nullators and norators, the circuit with the two added resistors do have the same behavior of the circuit in Fig. 6.

When designing the WDF model of the *Inverse System*, it is worth remembering that in a WDF structure we do not have direct access to potentials at nodes, as it happens with other circuit simulation methods, like the Modified Nodal Analysis, but just to port voltages (i.e., differences of potentials) [20]. In order to solve this problem, we add the two resistors with resistances $R_{\mathrm{rd}} = 100$ kΩ and $R_{\mathrm{ser}} = 1\Omega$ to the reference circuit in Fig. 6, as shown in Fig. 8. The resistor R_{rd} is added in parallel to the norator in order to simplify the reading of the signal $\widehat{V}_{\mathrm{in}}$ which is equal to the voltage across it. Notice that, irrespective of the resistance value, R_{rd} does not modify the behavior of the reference circuit in Fig. 6 because of the properties of the norator [19, 26]. On the other hand, the resistor R_{ser} is added in series to the nullator in order to combine it with the generator P_{out}, which can then be modeled as a resistive voltage source. This allows us to adapt the voltage source in the Wave Digital (WD) domain by breaking the local delay-free-loop that would otherwise arise if P_{out} were modeled as an ideal voltage source (in fact, ideal sources cannot be made reflection free in the WD domain [20]). Also the added resistor R_{ser} does not affect the behavior of the original circuit because of the properties of the nullator [19, 26].

The WDF realization of the *Inverse System* is shown in Fig. 9. As far as the WD modeling of the elements of the *Inverse System* is concerned, they are characterized by the same scattering relations used in the WDF implementation of the *Direct System* presented in [18]. The nonlinearities $Bl(x)$, $L_{\mathrm{e}}(x)$, and $C_{\mathrm{ms}}(x)$ are characterized by the same polynomial functions of the *Direct System* [18] and need to be updated at each sampling step, once an estimate of the

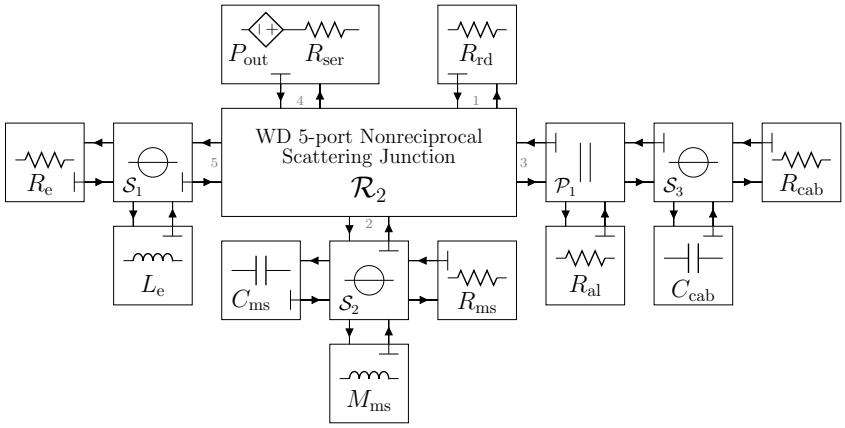

Figure 9: WDF realization of the *Inverse System*.

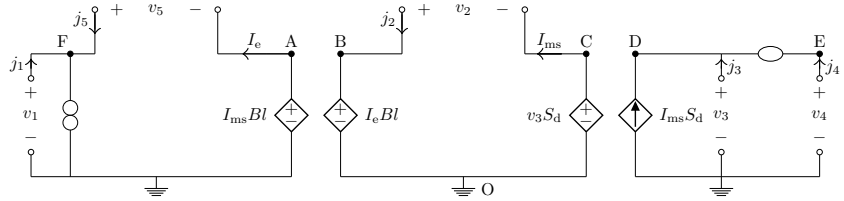

Figure 10: 5-port connection network implemented with WD $\mathcal{R}_2$ adaptor.

diaphragm displacement x is computed. Also the series and parallel junctions $\mathcal{S}_1$, $\mathcal{S}_2$, $\mathcal{S}_3$, and $\mathcal{P}_1$ are modeled as in the *Direct System*. In addition to R_{rd} and R_{ser}, the only new block of the WDF in Fig. 9 is the junction $\mathcal{R}_2$ implementing the 5-port non-reciprocal connection network in Fig. 10 that embeds a gyrator, a transformer, and a nullor. In Fig. 9 the port numbers of $\mathcal{R}_2$ are indicated in gray. The scattering matrix $\mathbf{S}_{\mathcal{R}_2}$ of the WD junction $\mathcal{R}_2$ is derived using the approach described in [22] obtaining

$$\mathbf{S}_{\mathcal{R}_2} = \begin{bmatrix} -1 & -\frac{2Z_5}{Bl} & -\frac{2(Bl^2+Z_2Z_5)}{BlS_{\text{d}}Z_3} & \frac{2(Bl^2+Z_3Z_5S_{\text{d}}^2+Z_2Z_5)}{BlS_{\text{d}}Z_3} & +2 \\ 0 & +1 & \frac{2Z_2}{S_{\text{d}}Z_3} & -\frac{2Z_2}{S_{\text{d}}Z_3} & 0 \\ 0 & 0 & -1 & +2 & 0 \\ 0 & 0 & 0 & +1 & 0 \\ 0 & -\frac{2Z_5}{Bl} & -\frac{2Z_2Z_5}{BlS_{\text{d}}Z_3} & \frac{2Z_5(Z_3S_{\text{d}}^2+Z_2)}{BlS_{\text{d}}Z_3} & +1 \end{bmatrix} \tag{2}$$

where $Z_1, \ldots, Z_5$ are the reference port resistances at the five ports of the junc-

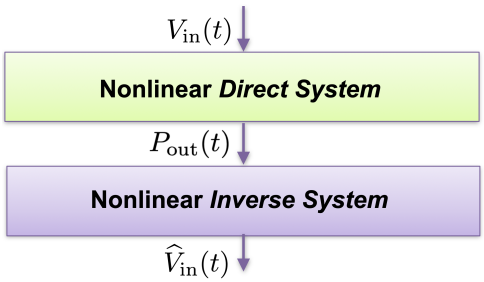

Figure 11: Processing structure for the validation of the nonlinear *Inverse System* block.

tion $\mathcal{R}_2$. The argument x of the $Bl(x)$ parameter in the coefficients of $\mathbf{S}_{\mathcal{R}_2}$ is omitted for the sake of compactness.

The WD structure in Fig. 9 is implemented similarly to the one designed for the *Direct System*; the leaves are all the adapted one-ports, the nodes are the series and the parallel adaptors while the root is $\mathcal{R}_2$.

4.1. Inverse System Model Validation

In order to validate the WDF implementation of the nonlinear *Inverse System*, we use the configuration shown in Fig. 11; we put the *Direct System* and the *Inverse System* in cascade and we verify whether the input signal of the *Direct System* V_{in} is the same of the output signal of the *Inverse System* named $\widehat{V}_{\text{in}}$, given the output signal of the *Direct System* P_{out} as input to the *Inverse System*.

In our experiments, we consider the two loudspeaker systems already described in the first part of this work [18] and characterized by the two drivers LaVoce FSF122.02-8 and LaVoce FSN020.71-4 of significantly different sizes. As in [18], the two loudspeakers will be referred to as Spk-1 and Spk-2. The circuit parameters are the same reported in Table 2 and Table 4 of [18]. The sampling frequency of the discrete-time simulations is $F_{\text{s}} = 96$ kHz.

Similarly to what done in [18], the input signals used in all the experiments of the manuscript are in the form

$$V_{\text{in}}(t) = A_{\text{in}} \frac{s_{\text{in}}(t)}{\text{rms}\{s_{\text{in}}(t)\}} \tag{3}$$

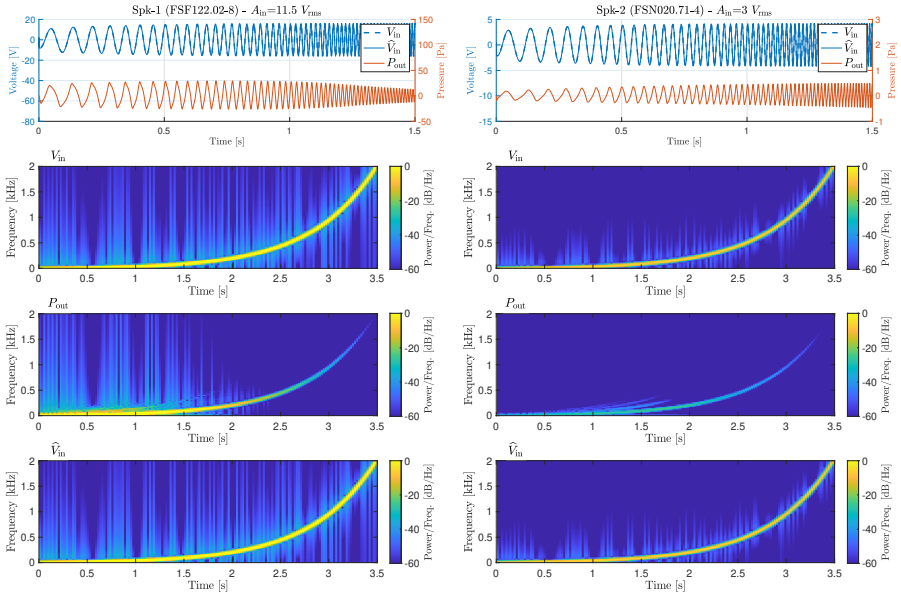

(a) (b)

Figure 12: *Inverse System* validation test. Comparisons between V_{in} and $\widehat{V}_{\text{in}}$ with reference to Fig. 11. Upper plots show comparisons in the time domain. The second row, the third row, and the fourth row of plots show the spectrograms of V_{in}, P_{out}, and $\widehat{V}_{\text{in}}$, respectively. (a) refers to Spk-1. (b) refers to Spk-2.

where A_{in} is an amplitude parameter in V_{rms}, rms$\{.\}$ is an operator returning the root mean square value of the argument. In this section, $s_{\text{in}}(t)$ is always an exponential sine sweep defined as [32]

$$s_{\text{in}}(t) = \sin\left[2\pi f_1 L \exp\left(\frac{t}{L}\right)\right], \tag{4}$$

where $L = \frac{T}{\log(f_2/f_1)}$, being $f_1 = 10$ Hz, $f_2 = 20$ kHz, and $T = 5$ s the initial frequency, the final frequency, and the duration of the sweep, respectively.

Fig. 12 contains the validation results. Fig. 12(a) refers to Spk-1 and $A_{\text{in}} = 11.5$ V_{rms}, while Fig. 12(b) refers to Spk-2 and $A_{\text{in}} = 3$ V_{rms}. The plots in the first row show a zoomed portion of the signals V_{in}, $\widehat{V}_{\text{in}}$, and P_{out} in the time domain. The plots in the second, the third, and the fourth rows, instead, show the spectrograms of V_{in}, P_{out}, and $\widehat{V}_{\text{in}}$, respectively. We can notice that, for both Spk-1 and Spk-2, V_{in} and $\widehat{V}_{\text{in}}$ are perfectly matching. This is evident from the plots in the time domain where V_{in} and $\widehat{V}_{\text{in}}$ are superimposed. Also looking at the spectrogram images, we notice that those in the second row are equal to those in the fourth row. It is worth highlighting that in the spectrograms of P_{out} additional curves are present due to the distortion introduced by the direct system, and that they nicely disappear in the spectrograms of $\widehat{V}_{\text{in}}$. The matching between V_{in} and $\widehat{V}_{\text{in}}$ is further verified by computing the Normalized Root Mean Square Error (NRMSE) between the two signals, which is NRMSE $= 5.3\times10^{-12}$ for Spk-1 and NRMSE $= 4.3 \times 10^{-14}$ for Spk-2.

5. Direct-Inverse-Direct Chain

Let us now describe the proposed loudspeaker virtualization method that is characterized by the signal flow in Fig. 13 referred to as *Direct-Inverse-Direct Chain* (DIDC). The DIDC is composed of three main input-output processing blocks. The two blocks above the gray horizontal line, i.e., the *Target Direct System* and the *Inverse System*, represent the digital preprocessing structure to be implemented, and they can be realized using the WDFs described in the first part [18] of this two-part work and in Section 4 of this manuscript. The

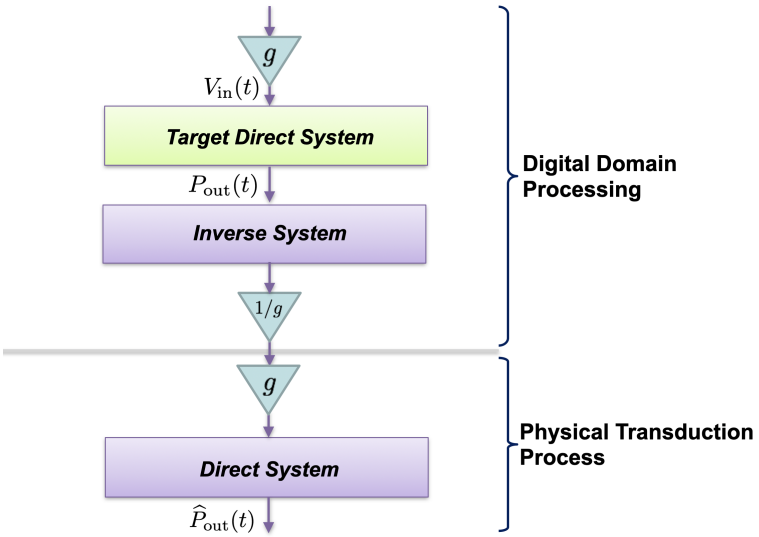

Figure 13: *Direct-Inverse-Direct Chain* representation.

last *Direct System* block below the gray line, instead, represents the actual loudspeaker, i.e., the physical transduction process. The scalar coefficient g is an amplification gain modeling the audio amplifier that is certainly present in real application scenarios. At the last step of the digital preprocessing stage the signal is rescaled by the coefficient $1/g$. The output signal $\widehat{P}_{\text{out}}$ of the physical *Direct System* is equal to the output signal P_{out} of the digital (virtual) *Target Direct System*, provided that the cascade of the *Inverse System* and the *Direct System* is equivalent to the identity operator. The design of the *Target Direct System* varies according to the application; in fact, the proposed virtualization method could be used for different tasks, including: loudspeaker equalization, loudspeaker linearization, or the forcing of a desired distortion behavior. It follows that, depending on the application, the *Target Direct System* might be linear or nonlinear. As a first example of virtualization, in the following section, we consider the task of loudspeaker linearization in which the *Target Direct System* is linear, while the *Inverse System* is nonlinear since it is ideally the exact inverse of the physical nonlinear *Direct System*. In the next section, instead, we will consider a further application of the proposed DIDC-based

algorithm in which the *Target Direct System* has a desired nonlinear behavior.

As far as the efficiency performance of the proposed DIDC-based method is concerned, the MATLAB implementation of the cascade of the *Target Direct System* and the *Inverse System* runs with an average execution time of approximately 0.66 μs per sample, which is lower than $T_\mathrm{s} = 1/F_\mathrm{s} = 1/(96\mathrm{kHz}) = 10.417$ μs. This means that the MATLAB implementations of the proposed DIDC-based algorithms discussed in the following sections can be executed on the fly.

6. DIDC-based Linearization of Loudspeakers

This section presents several experiments for the validation of the DIDC-based linearization algorithm. We will consider the two already described loudspeaker systems Spk-1 and Spk-2 in all the experiments. The *Target Direct System* is the WDF realization of the *linear loudspeaker model* described in Section 3 of [18]. The *Inverse System* is the nonlinear WDF described in Section 4 of this manuscript. Depending on the experiment, the *Direct System* is either one of the two physical loudspeakers Spk-1 and Spk-2 or the WDF model of nonlinear loudspeakers discussed in Section 5 of [18].

In case real loudspeakers are used, the measurement setup employed for sensing the output pressure of loudspeakers is the same described in Appendix A of [18]. The digital preprocessing algorithm, i.e., the digital portion of the DIDC including the *Target Direct System* and the *Inverse System*, is implemented in MATLAB and it is contained in the block "PC" of the scheme in Fig. A.9 of [18].

The scalar parameter g of the DIDC is set equal to the gain between the output voltage of the audio interface and the input voltage of the loudspeaker. With reference to the employed measurement setup, such a gain is 74.3 V/V in the frequency range from 5 Hz to 40 kHz.

The sampling frequency for digital preprocessing is $F_\mathrm{s} = 96$ kHz.

6.1. Simulation Results

Validation results discussed in this subsection refer to the case in which the physical *Direct System* is simulated using the WDF model of nonlinear loudspeakers discussed in Section 5 of [18]. The effectiveness of the proposed linearization algorithm based on predistortion is firstly verified by performing two tests: one referred to Spk-1 and one to Spk-2. In both cases we drive the DIDC with a sinusoidal signal V_{in} defined as in equation (3) with $s_{\text{in}}(t) = \sin(2\pi f_{\text{in}} t)$. We compare the power spectrum of the output pressure of the nonlinear *Direct System* when no preprocessing is performed and when the proposed DIDC-based precompensation algorithm is active, along with the corresponding values of Total Harmonic Distortion (THD). The simulation results are reported in Fig. 14; the plots on the left refer to Spk-1, while the plots on the right to Spk-2. The values of A_{in} and f_{in} in the two experiments are written on the plots. We can state that the proposed linearization algorithm works perfectly in both cases, since the harmonics are suppressed while preserving the content at the fundamental frequency f_{in}. The THD reduction, in fact, turns out to exceed 230 dB in the first experiment, and over 280 dB in the second experiment.

With the purpose of verifying that the proposed algorithm have similar performance also when input sinusoids V_{in} with different fundamental frequencies are considered, each subfigure in Fig. 15 shows a comparison between the THD curve of the output pressure of the nonlinear *Direct System* (blue line with circles indicated with "Non Compensated") and the THD curve of the output of the DIDC (red line with stars indicated with "Compensated") both as functions of frequency in the range $[10\ \text{Hz}, 3\ \text{kHz}]$. Fig. 15(a) refers to Spk-1 and the input sinusoids used to produce the THD curves have amplitude $A_{\text{in}} = 11.5\ \text{V}_{\text{rms}}$, while Fig. 15(b) refers to Spk-2 and the input sinusoids have amplitude $A_{\text{in}} = 3\ \text{V}_{\text{rms}}$.

6.2. Measurements

In this subsection the third block of the DIDC, i.e., the *Direct System*, is one of the two physical loudspeakers Spk-1 and Spk-2. The output pressure of the

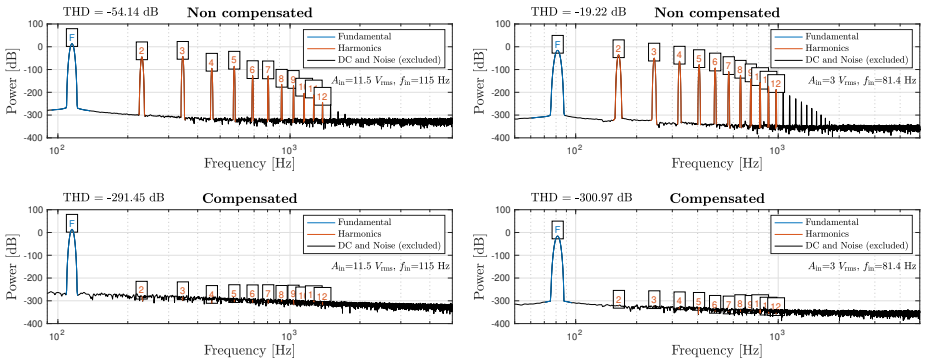

(a) Spk-1 (FSF122.02-8) (b) Spk-2 (FSN020.71-4)

Figure 14: DIDC-based linearization algorithm tested with simulated nonlinear *Direct System*. Upper subplots show the power spectra of the output pressure of the nonlinear *Direct System* when no preprocessing is performed. Lower subplots are obtained when the precompensation algorithm is active. (a) refers to Spk-1. (b) refers to Spk-2.

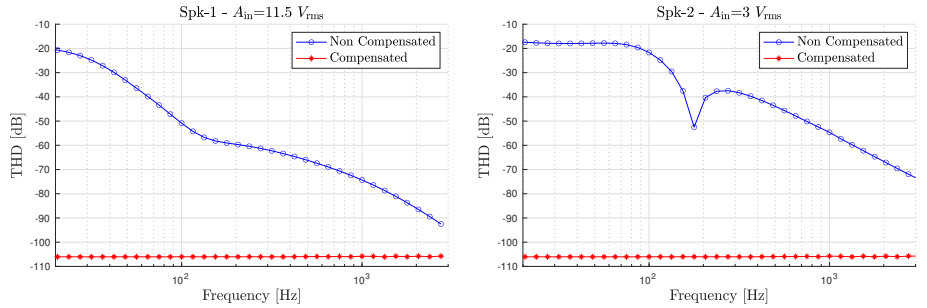

(a) Spk-1 (FSF122.02-8) (b) Spk-2 (FSN020.71-4)

Figure 15: DIDC-based linearization algorithm tested with simulated nonlinear *Direct System*. Both subfigures show THD curves of the output pressure of the nonlinear *Direct System* (blue line with circles) and of the output of the DIDC (red line with stars) as functions of frequency. (a) refers to Spk-1; input sinusoids have amplitude $A_{\text{in}} = 11.5\ V_{\text{rms}}$. (b) refers to Spk-2; input sinusoids have amplitude $A_{\text{in}} = 3\ \text{V}_{\text{rms}}$.

loudspeakers is sensed using the measurement setup described in Appendix A of [18]. Fig. 16 shows the results of the experiments for input sinusoids at different frequencies and with different amplitudes. Fig. 16(a) refers to Spk-1, while Fig. 16(b) refers to Spk-2. The left column of plots indicated with "Non Compensated" refers to the output pressure signals measured from the real loudspeakers in a configuration with no digital preprocessing. The left column of plots indicated with "Compensated" refers to the output pressure signals measured from the real loudspeakers when the DIDC-based linearization algorithm is active. The values of A_{in} and f_{in} for each experiment are written on the plots.

It is evident from Fig. 16 that even with real loudspeakers the DIDC-based linearization algorithm is effective in all the performed tests. In particular, in the experiments wherein the loudspeaker systems with no digital preprocessing are characterized by highest THD (i.e., the cases with highest amplitude A_{in} and lowest frequency f_{in}), the proposed algorithm reduces the THD of more than 20 dB for Spk-1, when $A_{\text{in}} = 11.5$ V_{rms} and $f_{\text{in}} = 28.75$ Hz, and of more than 25 dB for Spk-2, when $A_{\text{in}} = 3$ V_{rms} and $f_{\text{in}} = 81.4$ Hz.

6.3. DIDC Robustness to Parameter Uncertainty

So far we assumed that the optimal values of the nonlinear circuital model of the physical loudspeaker are known. Of course, this assumption is not valid in many application scenarios. In fact, although modern systems for the analysis of loudspeakers, such as the Klippel Analyzer [1], are characterized by high accuracy (as extensively confirmed by the results presented in [18]), the values of the parameters of the employed equivalent circuits can only be estimated with a certain degree of uncertainty. Moreover, short-term phenomena (such as temperature variations) and long-term phenomena (such as loudspeaker aging) can modify the loudspeaker behavior and cause the parameter values to further deviate from the optimal configuration. For this reason, in this subsection we perform a robustness analysis of the proposed linearization algorithm based on simulations. This means that, as third block of the DIDC, we use the WDF

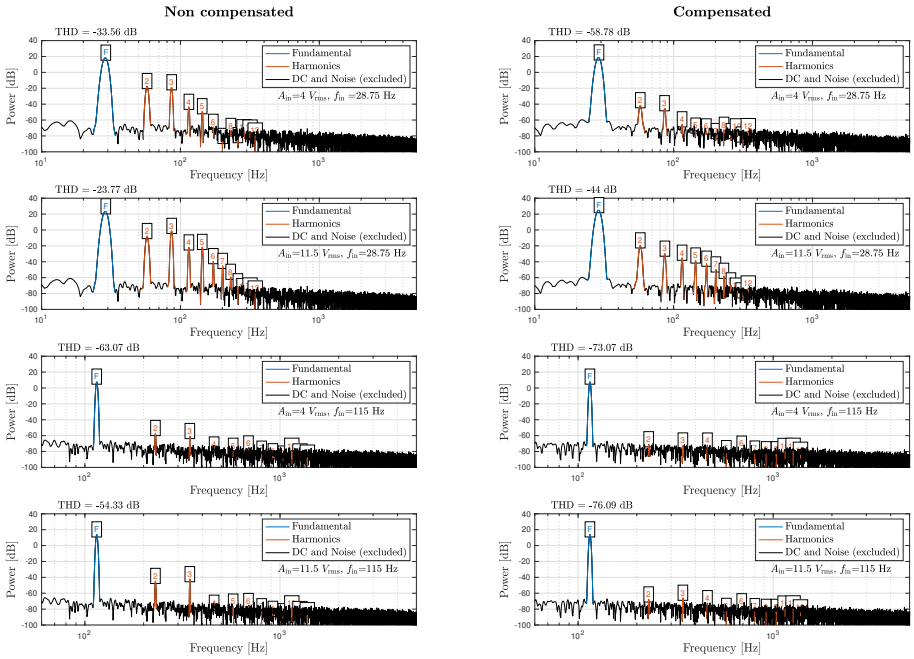

(a) Spk-1 (FSF122.02-8)

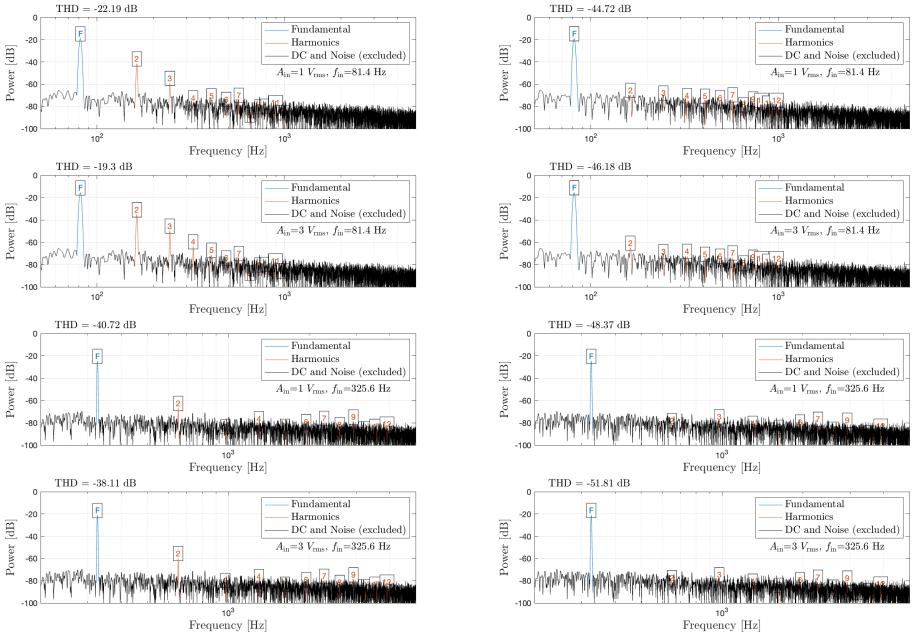

(b) Spk-2 (FSN020.71-4)

Figure 16: DIDC-based linearization algorithm tested with real loudspeakers. Plots on the left are the power spectra of the output pressure of the loudspeakers when no preprocessing is performed. Plots on the right show are obtained when the algorithm is active. (a) refers to Spk-1. (b) refers to Spk-2.

realization of the nonlinear *Direct System* already employed in Subsection 6.1 and we model each circuital parameter as follows

$$p_{\text{opt}} = p_{\text{est}} + p_{\text{err}} \tag{5}$$

where p_{opt} is the optimal parameter value, p_{est} is the measured parameter value, e.g., returned by the Klippel Analyzer system [1] or another system for the estimation of circuital parameters, while p_{err} is the measurement error. The parameters of the linear *Target Direct System* are set as in Table 2 of [18], while the parameters of the nonlinear *Inverse System* are set according to Table 2 and Table 4 of [18]. Each parameter of the third block of the DIDC (the nonlinear *Direct System*), instead, is computed as in equation (5), where p_{est} is taken from Table 2 and Table 4 of [18], while the error p_{err} that models the parameter uncertainty is a zero mean random variable with uniform distribution. We consider p_{err} to be uniformly distributed in the interval $[-0.05 \times p_{\text{est}}, 0.05 \times p_{\text{est}}]$, which means that each parameter is assumed to have a maximum percentage error of 5%.

As in the experiments of the previous two subsections, the input signals are sinusoids with amplitude A_{in} and fundamental frequency f_{in}. The first results of the robustness analysis are shown in Fig. 17 that contains two plots: Fig. 17(a) referred to an experiment with Spk-1 in which we set $A_{\text{in}} = 11.5$ V_{rms} and $f_{\text{in}} = 28.75$ Hz; and Fig. 17(b) referred to an experiment with Spk-2 in which we set $A_{\text{in}} = 3$ V_{rms} and $f_{\text{in}} = 81.4$ Hz. Both plots are obtained by running 1000 simulations of the single nonlinear *Direct System* and of the DIDC, and by computing the two resulting normalized histograms which approximate the probability density functions of THD (blue bars refer to the output of the single nonlinear *Direct System* and red bars refer to the output of the DIDC). In Fig. 17 we notice that, despite the discrepancy between the values of the circuital parameters of the nonlinear *Inverse System* and those of the nonlinear *Direct System*, the THD of the output signal of the DIDC is generally significantly lower than the THD of the output of the single nonlinear *Direct System*.

Such a behavior is confirmed by Fig. 18(a) and Fig. 18(b) that show com-

parisons between the THD curve of the output signal of the nonlinear *Direct System* (blue lines with circles and error bars) and the THD curve of the output of the DIDC (red lines with stars and error bars) both as functions of frequency in the range [10 Hz, 3 kHz]. Also in these experiments, circuital parameters are modeled as uniform random variables according to (5) and each parameter is assumed to have a maximum percentage error of 5%. For each f_{in} value, 1000 realizations of random parameter variables are considered. Circles and stars represent mean values, while vertical bars centered on the mean values represent the standard deviations over the 1000 realizations. Fig. 18(a) refers to Spk-1 and $A_{\text{in}} = 11.5$ V_{rms} for all input sinusoids. Fig. 18(b) refers to Spk-2 and $A_{\text{in}} = 3$ V_{rms} for all input sinusoids.

The previous two experiments related to Fig. 18(a) and Fig. 18(b) are repeated after increasing the maximum percentage error of each parameter of the nonlinear *Direct System* model to 10%; this means that the variable p_{err} referred to each parameter is uniformly distributed in the interval $[-0.1 \times p_{\text{est}}, 0.1 \times p_{\text{est}}]$. The results of these two further experiments are reported in Fig. 18(c) for Spk-1 and Fig. 18(d) for Spk-2.

Although the performance of the proposed algorithm is generally reduced with respect to the ideal scenario of Fig. 15 with no parameter uncertainty, we still achieve a THD reduction (averaged over frequency) of ≈ 20 dB for Spk-1 and of ≈ 22 dB for Spk-2 when the maximum percentage error of each parameter is 5%, and of ≈ 15 dB for Spk-1 and of ≈ 17 dB for Spk-2 when the maximum percentage error of each parameter is 10%. We can therefore conclude that the DIDC-based linearization algorithm proves to be remarkably beneficial even under considerable parameter uncertainty.

7. DIDC-based Virtualization of Loudspeakers

In this section, we consider a further application of the proposed DIDC-based algorithm in which the *Target Direct System* has a desired nonlinear behavior. The *Target Direct System* is therefore the WDF realization of the *nonlinear*

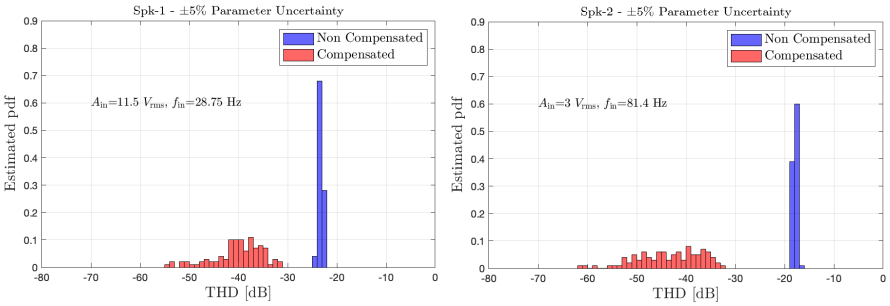

(a) Spk-1 (FSF122.02-8) (b) Spk-2 (FSN020.71-4)

Figure 17: Analysis of robustness to parameter uncertainty. Normalized histograms estimating the THD probability density functions referred to the output of the nonlinear *Direct System* (blue bars) and the output of the DIDC (red bars) obtained through 1000 simulations of both systems. (a) refers to Spk-1. (b) refers to Spk-2.

loudspeaker model described in Section 5 of [18] with modified parameters. Both for Spk-1 and for Spk-2, the parameters of nonlinearities of the target virtual loudspeaker are denoted by a ˜ and are expressed as functions of the measured parameters of real loudspeakers, as follows

$$\widetilde{Bl}_1 = Bl_1/100\,, \quad \widetilde{Bl}_2 = Bl_2/2\,, \quad \widetilde{Bl}_3 = Bl_3/100\,, \quad \widetilde{Bl}_4 = Bl_4/2\,, \tag{6}$$
$$\widetilde{K}_{\mathrm{ms1}} = K_{\mathrm{ms1}}/100\,, \quad \widetilde{K}_{\mathrm{ms2}} = K_{\mathrm{ms2}}/2\,, \quad \widetilde{K}_{\mathrm{ms3}} = K_{\mathrm{ms3}}/100\,, \quad \widetilde{K}_{\mathrm{ms4}} = K_{\mathrm{ms4}}/2\,,$$
$$\widetilde{L}_{\mathrm{e1}} = L_{\mathrm{e1}}/100\,, \quad \widetilde{L}_{\mathrm{e2}} = L_{\mathrm{e2}}/2\,, \quad \widetilde{L}_{\mathrm{e3}} = L_{\mathrm{e3}}/100\,, \quad \widetilde{L}_{\mathrm{e4}} = L_{\mathrm{e4}}/2\,.$$

All the other parameters of the *Target Direct System* that are not listed in (6) are those measured from real loudspeakers and reported in Table 2 of [18]. The *Inverse System* is the nonlinear WDF described in Section 4 of this manuscript. As in the previous section, depending on the experiment, the *Direct System* is either one of the two physical loudspeakers Spk-1 and Spk-2 or the WDF model of nonlinear loudspeakers discussed in Section 5 of [18]. Also here we always set $g = 74.3$ V/V and $F_{\mathrm{s}} = 96$ kHz.

In a first set of experiments, the *Direct System* is simulated using the nonlinear WDF model presented in [18]. As input signals V_{in} we use sinusoids with different fundamental frequencies f_{in} chosen by picking 24 frequency values per

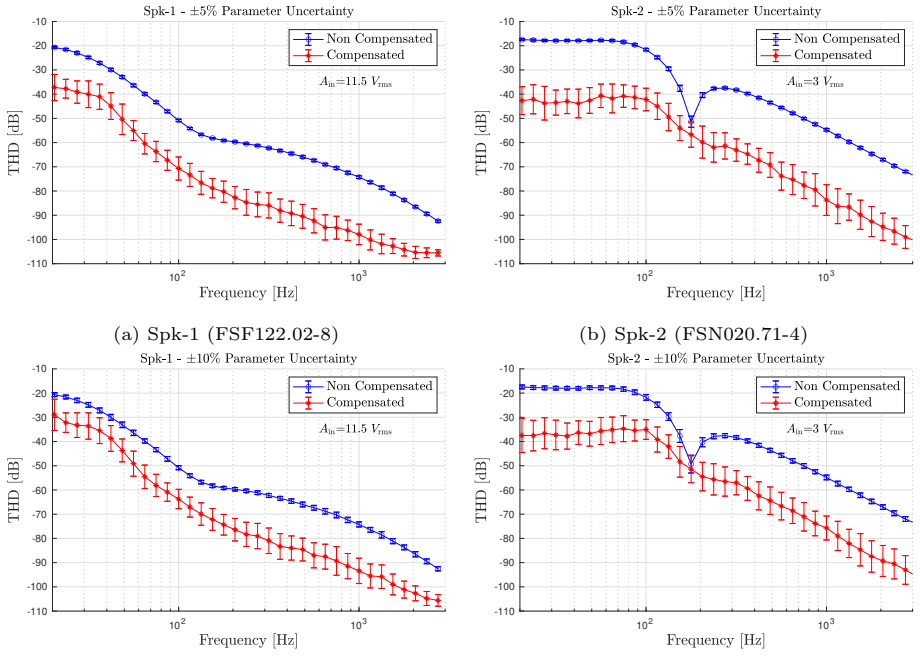

(a) Spk-1 (FSF122.02-8)

(b) Spk-2 (FSN020.71-4)

(c) Spk-1 (FSF122.02-8)

(d) Spk-2 (FSN020.71-4)

Figure 18: Analysis of robustness to parameter uncertainty. THD curves of the output signal of the nonlinear *Direct System* (blue lines with circles) and of the output of the DIDC (red lines with stars) as functions of frequency when circuital parameters of the *Direct System* are modeled as random variables. For each fundamental frequency f_{in}, circles and stars represent mean values, while vertical bars centered on the mean values represent the standard deviations over 1000 realizations. (a) and (c) refer to Spk-1. (b) and (d) refer to Spk-2. (a) and (b) are obtained with a parameter uncertainty of 5%, while (c) and (d) of 10%.

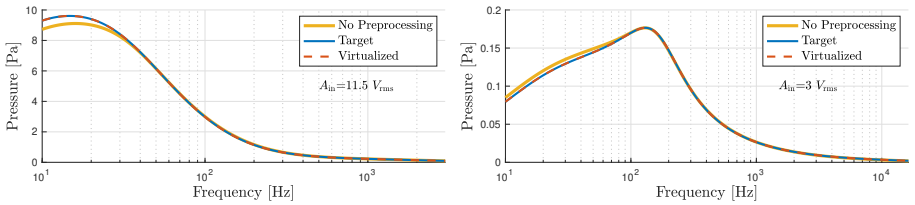

(a) Spk-1 (FSF122.02-8)

(b) Spk-2 (FSN020.71-4)

Figure 19: DIDC-based virtualization tests in which the *Direct System*, i.e., the third block of the DIDC, is simulated. Amplitude responses of the output pressure signal of: the *Direct System* when the virtualization algorithm is not active ("No Preprocessing"), the *Target Direct System* ("Target"), and the *Direct System* when the DIDC-based virtualization algorithm is active ("Virtualized"). (a) refers to Spk-1. (b) refers to Spk-2.

octave. The resulting signals are used to estimate the amplitude response of the output pressure in different configurations as shown in Fig. 19. The line indicated with "No Preprocessing" is the amplitude response of the output of the *Direct System* when the virtualization algorithm is not active. The line indicated with "Target" is the amplitude response of the output of the *Target Direct System*, i.e., the first block of the DIDC. The line indicated with "Virtualized" is the amplitude response of the output of the *Direct System* when the DIDC-based virtualization algorithm is active. Fig. 19(a) refers to Spk-1, while Fig. 19(b) to Spk-2. The values of the amplitude parameter A_{in} for each experiment are reported on the plots. We notice that in both cases the virtualized loudspeaker is characterized by an output amplitude response that is superimposed to the one of the *Target Direct System*.

The second set of experiments is similar to the first one, but we substitute the simulated *Direct System* (i.e., the third block of the DIDC) with one of the two real loudspeakers Spk-1 or Spk-2, again using the measurement setup described in Appendix A of [18]. The results are shown in Fig. 20. We notice that both in the case of Spk-1 (Fig. 20(a)) and of Spk-2 (Fig. 20(b)), the output signal of the virtualized loudspeaker matches that of the *Target Direct System*.

In the third set of experiments, we use the exponential sine sweep defined in

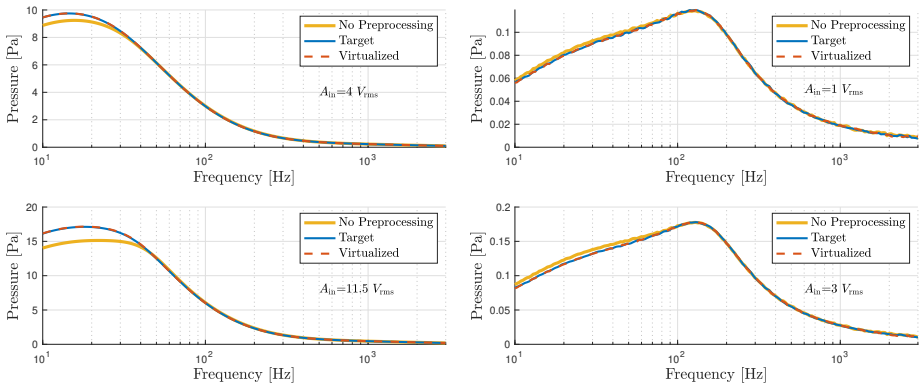

(a) Spk-1 (FSF122.02-8) (b) Spk-2 (FSN020.71-4)

Figure 20: DIDC-based virtualization tests in which the *Direct System*, i.e., the third block of the DIDC, is a real loudspeaker. Amplitude responses of the output pressure signal of: the *Direct System* when the virtualization algorithm is not active ("No Preprocessing"), the *Target Direct System* ("Target"), and the *Direct System* when the DIDC-based virtualization algorithm is active ("Virtualized"). (a) refers to Spk-1. (b) refers to Spk-2.

equations (3) and (4) as input signal V_{in}. The *Direct System* is again simulated using the nonlinear WDF model presented in [18]. The results are shown in Fig. 21. Upper plots show time domain comparisons between the output of the *Target Direct System* and the output of the *Direct System* when the virtualization algorithm is active. The same two signals are represented below using spectrograms. Spectrograms in the second row show P_{out}, which is the output of the *Target Direct System*. Spectrogram in the third row show $\widehat{P}_{\text{out}}$, which is the output of the DIDC. Fig. 21(a) refers to Spk-1, while Fig. 21(b) refers to Spk-2. The values of the amplitude parameter A_{in} are reported in the titles of subfigures. We notice that, in both cases, P_{out} and $\widehat{P}_{\text{out}}$ are superimposed in the time domain and their spectrogram images look the same. The matching between P_{out} and $\widehat{P}_{\text{out}}$ is further verified by computing the NRMSE between the two signals, which is NRMSE $= 1.6\times10^{-13}$ for Spk-1 and NRMSE $= 5.4\times10^{-13}$ for Spk-2.

The fourth set of experiments is similar to the third one, but we substitute the simulated *Direct System* (i.e., the third block of the DIDC) with one of the

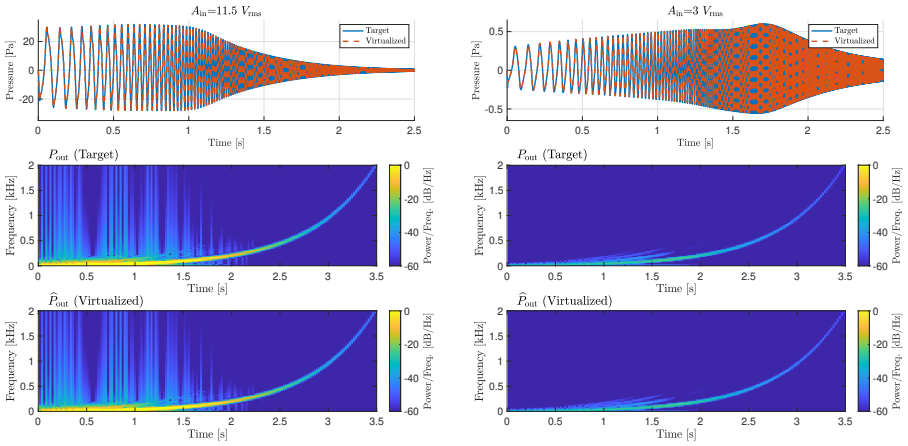

(a) Spk-1 (FSF122.02-8) (b) Spk-2 (FSN020.71-4)

Figure 21: DIDC-based virtualization tests in which the *Direct System*, i.e., the third block of the DIDC, is simulated. Comparisons between P_{out} and $\widehat{P}_{\text{out}}$. Upper plots show comparisons in the time domain. The second row and the third row of plots show the spectrograms of P_{out} and $\widehat{P}_{\text{out}}$, respectively. (a) refers to Spk-1. (b) refers to Spk-2.

two real loudspeakers Spk-1 or Spk-2. The results are shown in Fig. 22. We notice that both in the cases of Spk-1 (Fig. 22(a) and Fig. 22(c)) and of Spk-2 (Fig. 22(b) and Fig. 22(d)), the output signal of the virtualized loudspeaker matches that of the *Target Direct System*. The matching between P_{out} and $\widehat{P}_{\text{out}}$ is further verified by computing the NRMSE between the two signals for each experiment. We get: NRMSE $= 0.0024$ for Spk-1 and $A_{\text{in}} = 4$ V_{rms}, NRMSE $= 0.0041$ for Spk-1 and $A_{\text{in}} = 11.5$ V_{rms}, NRMSE $= 0.1119$ for Spk-2 and $A_{\text{in}} = 1$ V_{rms}, and NRMSE $= 0.0451$ for Spk-2 and $A_{\text{in}} = 3$ V_{rms}.

8. Conclusions and Future Work

In this manuscript, the second of a two-part work, we proposed a signal processing method operating in the discrete-time domain, for *virtualizing* the behavior of physical dynamic loudspeakers. The transduction process is here described using the nonlinear circuital model that was extensively discussed in the first manuscript [18] of this two-part work. This model includes an electri-

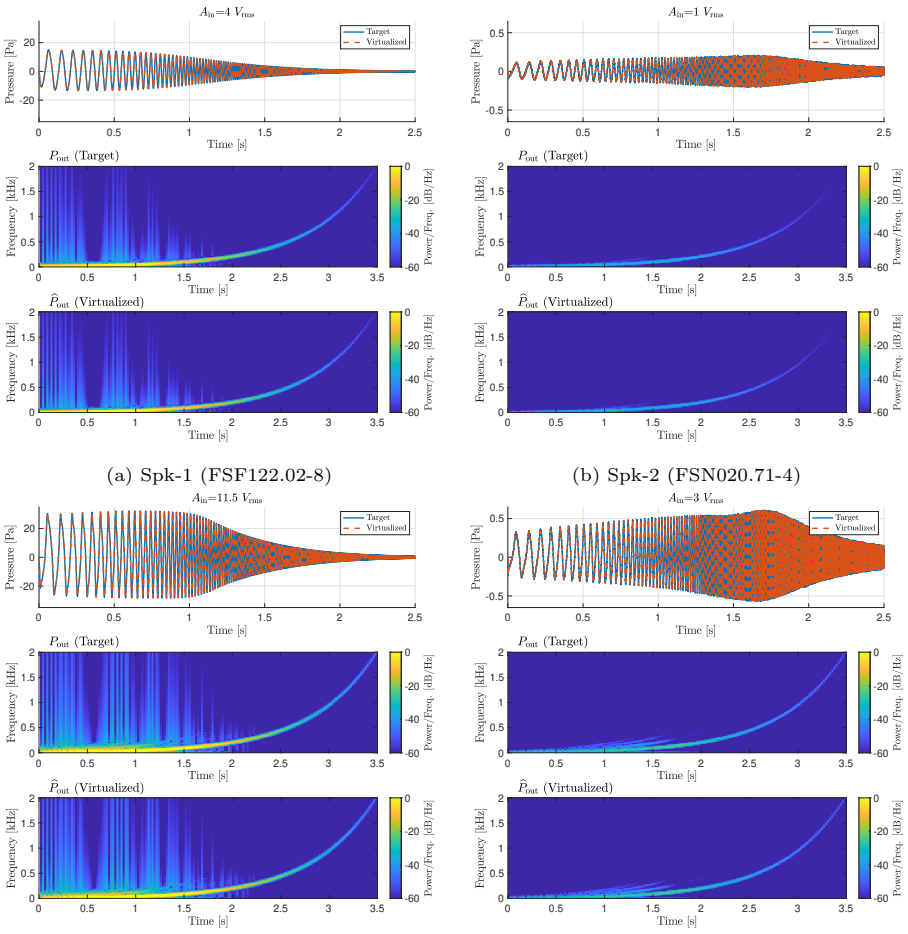

(a) Spk-1 (FSF122.02-8)

(b) Spk-2 (FSN020.71-4)

(c) Spk-1 (FSF122.02-8)

(d) Spk-2 (FSN020.71-4)

Figure 22: DIDC-based virtualization tests in which the *Direct System*, i.e., the third block of the DIDC, is a real loudspeaker. Comparisons between P_{out} and $\widehat{P}_{\text{out}}$. Upper plots show comparisons in the time domain. The second row and the third row of plots show the spectrograms of P_{out} and $\widehat{P}_{\text{out}}$, respectively. (a) and (c) refer to Spk-1. (b) and (d) refer to Spk-2.

cal part, driven by an input voltage signal; a mechanical part; and an acoustic part, which includes the output pressure signal. The proposed loudspeaker virtualization method relies on the *exact* inversion of the reference circuital model of the transducer. The inverse model is, in fact, obtain by adding an ideal two-port circuit element called *nullor* to the electrical equivalent of the loudspeaker. In particular, the virtualization algorithm is based on the so called *Direct-Inverse-Direct Chain* (DIDC) composed of the digital *Target Direct System*, which models the desired loudspeaker behavior; the digital nonlinear *Inverse System*; and the actual physical *Direct System*. The *Target Direct System* and the *Inverse System* are implemented in the WD domain in a fully explicit fashion (i.e., without any iterative solver) by exploiting both traditional WDF principles and novel discretization techniques that were never discussed in the literature. Depending on the virtualization application (e.g., equalization, introduction of desired distortion, linearization) the *Target Direct System* might be linear or nonlinear. In this manuscript, we discussed one of the most challenging virtualization applications, that is *loudspeaker linearization*, in which the *Target Direct System* is linear. We also discussed another application of the proposed DIDC-based virtualization approach in which the *Target Direct System* is characterized by a nonlinear behavior different from the one of the physical loudspeaker. The proposed algorithms have been extensively validated through experiments based on simulations and applications to real loudspeakers.

As far as future works are concerned, we are planning to test the proposed DIDC-based virtualization approach with other electrical equivalents of loudspeaker systems modeling further transduction nonidealities that have not been considered in this work [33].

9. Acknowledgements

The research work presented in this article was founded by Elettromedia s.p.a., Strada Regina km 3.500, 62018 Potenza Picena (MC), Italy.

References

[1] W. Klippel, Distortion analyzer-a new tool for assessing and improving electrodynamic transducer, in: Audio Engineering Society Convention 108, 2000.
URL http://www.aes.org/e-lib/browse.cfm?elib=9229

[2] W. Klippel, Compensation for nonlinear distortion of horn loudspeakers by digital signal processing, J. Audio Eng. Soc 44 (11) (1996) 964–972.
URL http://www.aes.org/e-lib/browse.cfm?elib=7878

[3] J. Suykens, J. Vandewalle, J. Van Ginderdeuren, Feedback linearization of nonlinear distortion in electrodynamic loudspeakers, Journal of the Audio Engineering Society 43 (9) (1995) 690–694.
URL http://www.aes.org/e-lib/browse.cfm?elib=7930

[4] P. M. Brunet, G. S. Kubota, Nonlinear control of loudspeaker based on output flatness and trajectory planning, in: Audio Engineering Society Convention 147, 2019.
URL http://www.aes.org/e-lib/browse.cfm?elib=20614

[5] J. Lazar, P. M. Brunet, Reluctance force compensation for the nonlinear control of a loudspeaker, in: Audio Engineering Society Convention 149, 2020.
URL http://www.aes.org/e-lib/browse.cfm?elib=20962

[6] W. Klippel, The Mirror Filter-A new basis for reducing nonlinear distortion and equalizing response in woofer systems, Journal of the Audio Engineering Society 40 (9) (1992) 675–691.
URL http://www.aes.org/e-lib/browse.cfm?elib=7034

[7] W. Frank, R. Reger, U. Appel, Realtime loudspeaker linearization, in: IEEE Winter Workshop on Nonlinear Digital Signal Processing, 1993, pp. $2.1_3.1 - -2.1_3.5$. doi:10.1109/NDSP.1993.767693.

[8] H. Merabti, D. Massicotte, W.-P. Zhu, Electrodynamic loudspeaker linearization using a low complexity pth-order inverse nonlinear filter, in: 2019 IEEE International Symposium on Signal Processing and Information Technology (ISSPIT), 2019, pp. 1–5. doi:10.1109/ISSPIT47144.2019.9001831.

[9] P. M. Brunet, Y. Li, G. S. Kubota, A. Mariajohn, Application of ai techniques for nonlinear control of loudspeakers, in: Audio Engineering Society Convention 151, 2021.
URL http://www.aes.org/e-lib/browse.cfm?elib=21499

[10] B. R. Pedersen, P. Rubak, Linearization of nonlinear loudspeakers, in: Audio Engineering Society Convention 121, 2006.
URL http://www.aes.org/e-lib/browse.cfm?elib=13775

[11] S. S. Payal, V. J. Mathews, A. Iyer, R. Lambert, J. Hutchings, Equalization of excursion and current-dependent nonlinearities in loudspeakers, in: 2014 IEEE International Conference on Acoustics, Speech and Signal Processing (ICASSP), 2014, pp. 6697–6701. doi:10.1109/ICASSP.2014.6854896.

[12] A. Falaize, N. Papazoglou, T. Hélie, N. Lopes, Compensation of loudspeaker's nonlinearities based on flatness and port-Hamiltonian approach, in: 22ème Congrès Français de Mécanique, Association Française de Mécanique, Lyon, France, 2015.
URL https://hal.archives-ouvertes.fr/hal-01245632

[13] X. Tian, W. Liu, X. Feng, Y. Shen, Compensation of nonlinear distortion in loudspeakers considering nonlinear viscoelasticity of the suspension, Journal of the Audio Engineering Society 69 (3) (2021) 204–210. doi:https://doi.org/10.17743/jaes.2020.0072.

[14] W. Klippel, Direct feedback linearization of nonlinear loudspeaker systems, Journal of the Audio Engineering Society 46 (6) (1998) 499–507.
URL http://www.aes.org/e-lib/browse.cfm?elib=12142

[15] D. Franken, K. Meerkotter, J. Wassmuth, Observer-based feedback linearization of dynamic loudspeakers with ac amplifiers, IEEE Transactions on Speech and Audio Processing 13 (2) (2005) 233–242. doi:10.1109/TSA.2004.841043.

[16] P. Dziechciński, Comparison of digital loudspeaker-equalization techniques, Archives of Acoustics 30 (2).
URL https://acoustics.ippt.pan.pl/index.php/aa/article/view/513

[17] X. Li, Z. Cai, C. Zheng, X. Li, Equalization of loudspeaker response using balanced model truncation, The Journal of the Acoustical Society of America 137 (4) (2015) EL241–EL247. doi:10.1121/1.4914946.

[18] A. Bernardini, L. Bianchi, A. Sarti, Loudspeaker Virtualization–Part I: Digital Modeling and Implementation of the Nonlinear Transducer Equivalent Circuit, accepted for publication in Signal Processing.

[19] H. J. Carlin, Singular network elements, IEEE Trans. Circuit Theory 11 (1) (1964) 67–72.

[20] A. Fettweis, Wave digital filters: Theory and practice, Proc. IEEE 74 (2) (1986) 270–327.

[21] A. Bernardini, K. J. Werner, J. O. Smith, A. Sarti, Generalized wave digital filter realizations of arbitrary reciprocal connection networks, IEEE Transactions on Circuits and Systems I: Regular Papers 66 (2) (2019) 694–707. doi:10.1109/TCSI.2018.2867508.

[22] K. J. Werner, A. Bernardini, J. O. Smith, A. Sarti, Modeling circuits with arbitrary topologies and active linear multiports using wave digital filters, IEEE Transactions on Circuits and Systems I: Regular Papers 65 (12) (2018) 4233–4246. doi:10.1109/TCSI.2018.2837912.

[23] A. Bernardini, P. Maffezzoni, A. Sarti, Linear multistep discretization methods with variable step-size in nonlinear wave digital structures for

virtual analog modeling, IEEE/ACM Transactions on Audio, Speech, and Language Processing 27 (11) (2019) 1763–1776. doi:10.1109/TASLP.2019.2931759.

[24] A. Leuciuc, The realization of inverse system for circuits containing nullors with applications in chaos synchronization, International Journal of Circuit Theory and Applications 26 (1) (1998) 1–12.

[25] A. Davies, The significance of nullators, norators and nullors in active-network theory, Radio and Electronic Engineer 34 (1967) 259–267(8). URL https://digital-library.theiet.org/content/journals/10.1049/ree.1967.0095

[26] J. Vandewalle, J. A. Nossek, Nullators and norators in circuits education: A benefit or an obstacle?, in: 2011 IEEE Int. Symp. Circuits and Systems (ISCAS), 2011, pp. 349–352. doi:10.1109/ISCAS.2011.5937574.

[27] R. Giampiccolo, M. G. De Bari, A. Bernardini, A. Sarti, Wave digital modeling and implementation of nonlinear audio circuits with nullors, IEEE/ACM Transactions on Audio, Speech, and Language Processing (2021) 1–1doi:10.1109/TASLP.2021.3120627.

[28] F. Bohme, W. Schwarz, The chaotizer-dechaotizer-channel, IEEE Transactions on Circuits and Systems I: Fundamental Theory and Applications 43 (7) (1996) 596–599.

[29] U. Feldmann, M. Hasler, W. Schwarz, Communication by chaotic signals: the inverse system approach, International Journal of Circuit Theory and Applications 24 (5) (1996) 551–579.

[30] L. M. Pecora, T. L. Carroll, Synchronization of chaotic systems, Chaos: An Interdisciplinary Journal of Nonlinear Science 25 (9) (2015) 0976111–09761112.

[31] A. Bernardini, A. Sarti, Towards inverse virtual analog modeling, in: Proc. 22nd Int. Conf. Digital Audio Effects (DAFx 2019), Birmingham, UK, 2019.

[32] A. Novak, L. Simon, F. Kadlec, P. Lotton, Nonlinear system identification using exponential swept-sine signal, IEEE Trans. Instrum. Meas. 59 (8) (2010) 2220–2229.

[33] W. Klippel, Tutorial: Loudspeaker nonlinearities—causes, parameters, symptoms, J. Audio Eng. Soc 54 (10) (2006) 907–939.
URL http://www.aes.org/e-lib/browse.cfm?elib=13881